energies

MDPI

Article

Hydrodynamic Characteristic Around the Riprap Protection of Monopile Wind Power Foundation with Scour Pit During Scour

Tongshun Yu [1,2,*], Li Wang [1], Congbao Mei [1,3] and Xiaofeng Dong [4]

[1] College of Engineering, Ocean University of China, Qingdao 266100, China; warwick2001@163.com (L.W.); meicongbao@163.com (C.M.)
[2] Shandong Provincial Key Laboratory of Ocean Engineering, Qingdao 266100, China
[3] Emeishan City Transportation Bureau, Emeishan 614200, China
[4] School of Civil Engineering, Tianjin University, Tianjin 300350, China; xiaofeng.dong@tju.edu.cn
* Correspondence: tshyu707@ouc.edu.cn

Abstract

Riprap protection is widely used in offshore wind power foundations. The boundary of riprap will change and affect the hydrodynamics around the foundation during scour. In this study, the experiment was conducted to obtain the topographic data of the riprap failure process. Then, a numerical model of current-pile-riprap-seabed interaction was set using the data to explore the hydrodynamic characteristics around the monopile during the process of stone moving under the action of current. The numerical model is verified through theory and test data. The results show that compared with an unprotected foundation, the maximum flow velocity and range of horseshoe vortex around the monopile with intact riprap will increase, while pressure around the monopile will decrease. During the process of scour, the riprap will sink and be scoured, resulting in increased water cross-section and a velocity decrease of 9.32% to 17.05%. In the process of riprap damage, the height of the diving flow increases, and the horseshoe vortex continuously decreases. The wake vortex near the surface remains stable during the process, while the wake vortex near bed gradually shrinks and disappears. Meanwhile, the pressure around the monopile increases, with maximum pressure increasing by 3.38 times.

Keywords: monopile; scour; riprap protection; horseshoe vortex; wake vortex

Academic Editor: Frede Blaabjerg

Received: 17 September 2025
Revised: 28 October 2025
Accepted: 31 October 2025
Published: 3 November 2025

Citation: Yu, T.; Wang, L.; Mei, C.; Dong, X. Hydrodynamic Characteristic Around the Riprap Protection of Monopile Wind Power Foundation with Scour Pit During Scour. *Energies* **2025**, *18*, 5792. https://doi.org/10.3390/en18215792

1. Introduction

With the global emphasis on offshore renewable energy, the construction of offshore wind power is in full swing. Monopile foundation is widely used in major wind farms due to its advantages of simple construction and low cost [1]. As the offshore wind power industry develops in deeper waters, wind turbines with larger structures and capacities have become more common, posing greater challenges for the structural design and scour protection of monopile foundations [2]. Offshore scour protection is a study field with a wide margin of development, but crucial for the future of the offshore renewable energy sector, thus pointing out key challenges and major opportunities for future research [3]. In order to cope with the scour problem induced by wave and current [4], many scholars and engineers have proposed various scour protection measures, such as riprap [5], column body hole protection [6], and sleeve protection [7,8]. Among these, riprap protection is widely used due to its advantages of simple construction and convenient materials.

Riprap cannot achieve scour protection once and for all. Under the action of a complex Marine environment, the riprap around the pile foundation will be damaged. Scholars

have carried out research on the damage mechanism of riprap protection. Through an experimental study, Parola [9] determined the critical condition of riprap displacement on the seabed surface around the pile foundation. Chiew [10] conducted a study on the stability of riprap around pile foundations and analyzed the failure mechanisms of riprap protection under clear-water scour conditions, based on experimental research. Three modes of failure have been summarized: riprap shear failure, winnowing failure, and edge failure. Chiew and Lim [11] changed the bed condition to study the stability of riprap and found the destruction mechanism under live-bed conditions, namely disintegration failure and embedment failure. Lauchlan and Melville [12] summarized the above mechanisms of riprap destruction and proposed a pier riprap size-prediction equation, including a parameter to account for placement level. Lim and Chiew [13] proposed a maximum embedment velocity, which defines a critical flow velocity at which all riprap layers, irrespective of the characteristic parameters, will fail. Nielsen et al. [14] described the mechanisms of the sinking of a scour protection adjacent to a monopile, together with the determination of the equilibrium sinking depth in various wave and combined wave and current conditions based on physical model tests.

Nielsen [15] found that a larger pile diameter relative to the size of the protection stones will cause a larger sinking and that two layers of stones will decrease the sinking relative to one layer of stones with the same size. Petersen found that the equilibrium scour pit depth and length dimensions were related to the pile diameter and the ratio of protection thickness to width [16]. Early movement first appeared in the pile wake area, with no significant influence on the scour protection system, when the horseshoe vortex mobilizes the cover stones and immediately causes severe damage to the scour protection [17]. In some cases, the flow interaction with the protection causes edge scour or secondary scour in the seabed around the protection, and this scour is deeper than the unprotected case [18]. Almeida and Martin [19] conducted a study to determine the influence of length, width, and protrusion of noncontinuous riprap protections on shear failure conditions. They found that incipient motion conditions of transverse (cross-sectional) protections are strongly influenced by both the protrusion and length of bed protection, which indicates that stability significantly increases as protection length increases and decreases as protrusion increases. In the case of longitudinal protections, almost the same failure conditions were found as in the case of continuous protection. Furthermore, these conditions are unrelated to the width of the protection. Tang et al. [20] found a strong correlation between vibration amplitude and subsidence depth in front of the monopile, with larger riprap sizes proving more effective at resisting subsidence.

DeVos et al. [21] studied the size of riprap required for the protective measures of riprap under scour, put forward the design formula for determining the size of the required stone size, and adjusted it by waves, so that the design formula is also applicable to irregular waves. On this basis, DeVos et al. [22] obtained a more economical design by allowing some movement of the top-layer stones of the scour protection. Richardson et al. [23] suggested that the stone-throwing protection should be at least twice the pile width and proposed a formula for determining the stone size, which was further adopted by the US Highway Administration. Lagasse [24] proposed three types of stone-throwing layer arrangement, i.e., placing rock on the surface of the riverbed, in a scour pit, or in a hand-excavated pit near the foundation, and below a certain depth from the mean riverbed elevation.

It can be seen that the research on the protection of riprap basically focuses on the protection effect, scour depth, and damage mechanism, while there are no studies on the hydrodynamic characteristics of riprap destruction. In fact, riprap will lead to significant changes in the boundary conditions of the seabed where the pile foundation is located in the scour process, which will then affect the hydrodynamic characteristics and scour

effect around the pile foundation. Therefore, it is necessary to conduct research on the hydrodynamic characteristics of pile foundations under the complex seabed boundaries of a riprap—protected scour pit under the action of current. The test conditions limit the applicability of the physical model test, making it difficult to simulate a high Reynolds number environment [25]. Thus, Physical model tests and numerical simulations were used in this study to study the hydrodynamic characteristics of pile foundations. Other sections of this paper are presented as follows: Section 2 contains a description of the test facility and experimental setup. Section 3 describes the process of building and verifying the numerical model. Section 4 details the change in the hydrodynamic characteristics around the pile foundation at different stages of scour. Section 5 is the summary and the conclusion.

2. Physical Modeling Experiment

2.1. Experimental Setup

This experiment was conducted in the wave-current flume of the Engineering Hydrodynamics Laboratory, Ocean University of China. The prototype wind farm is the Three Gorges New Energy Wind Farm. The pile foundation, with a diameter of 3.9 m, was located at a water depth of 9 m and was experiencing a maximum flow velocity of 3 m/s. The gravity similarity criterion was employed in the experiment, and the corresponding model scale ratios are indicated in Table 1. The diameter of the pile was 6.5 cm in the experiment. The water depth of the experiment was 0.15 m, and the flow velocity was 0.387 m/s.

Table 1. Model scale ratio.

Type	Length Scale Ratio	Time Scale Ratio	Force Scale Ratio
Value	60	7.74	216,000

A physical model picture and the model size diagram are shown in Figure 1. The pile foundation consisted of an acrylic plate, and five pressure measuring points were arranged on both the front and back sides. The flow pressure on the pile foundation was measured using a pulsatile pressure sensor [26] at the specified measuring points in the physical model test, and the distances between these pressure measuring points and the water surface are listed in Table 2.

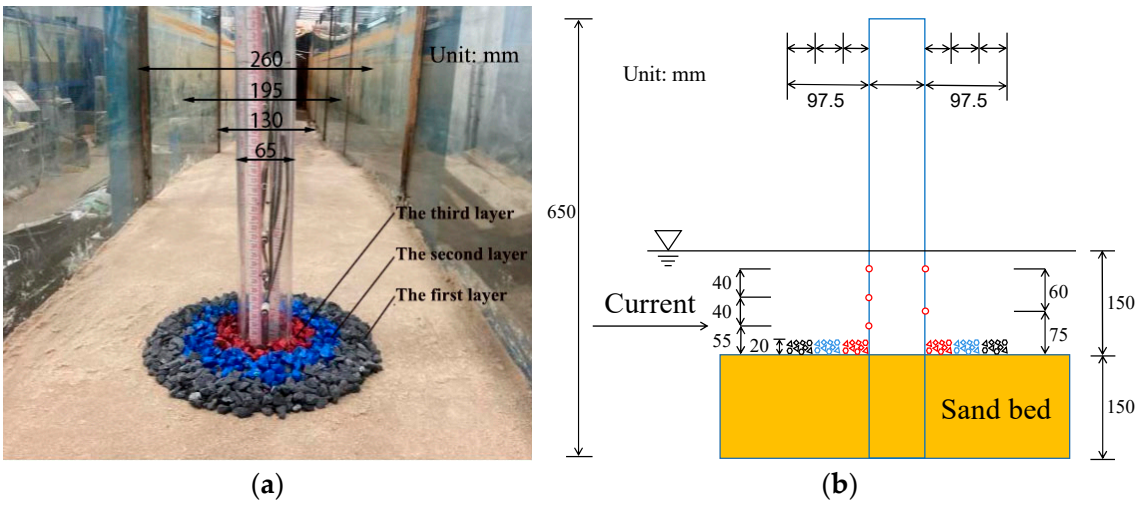

(**a**) (**b**)

Figure 1. The layout of the physical model experiment. (**a**) Physical model picture. (**b**) Physical model size diagram.

Table 2. Distance from the pressure measuring point to the static water surface.

Position	Point	Y (m)
Front of pile	*P1*	0.015
	P2	0.055
	P3	0.095
Back of pile	*P4*	0.015
	P5	0.075

In the middle of the flume, a 4 m × 0.6 m × 0.15 m horizontal sandy seabed was arranged, with a 1:10 slope on both sides. The model was placed in the middle of the seabed, with its lower part buried in the sediment. The specific seabed design, model, and equipment layout are shown in Figure 2.

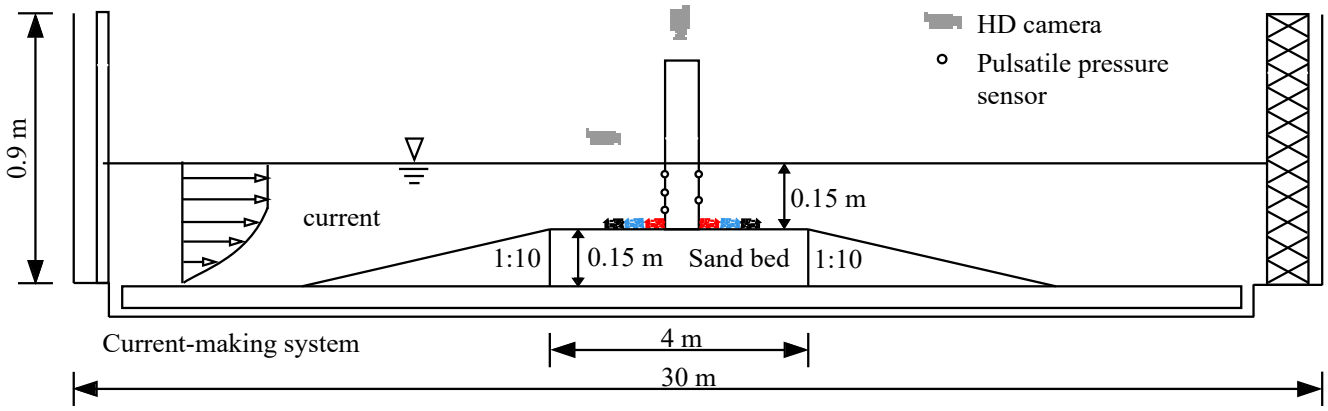

Figure 2. Schematic diagram of the flume test.

According to the recommendation of Richardson and Davis [23], the size of riprap has been recommended as follows:

$$\frac{d_{r50}}{y} = \frac{0.346 f_1^2 f_2^2}{S_s - 1} F_r^2 \quad (1)$$

$$F_r = \frac{v}{\sqrt{gy}} \quad (2)$$

where S_S is the specific gravity of bed material, generally 2.65 kN/m^3; v is the constant flow velocity; f_1 is the coefficient for the abutment shape, f_1 = 1.5 for circle and f_1 = 1.7 for rectangle; f_2 is the coefficient for the angle of embankment to flow, generally 0.9–1.7. When the pier is set on the river channel, f_2 = 0.9, and f_2 = 1.7 on the river bend; g is the gravity acceleration, 9.8 m/s^2; y is the flow depth (m); d_{r50} is the median diameter of riprap (m).

In this experiment, the prototype sand was used, and its median particle size is 0.129 mm, as shown in Figure 3. The riprap is made of limestone gravel, and the median diameter is 9 mm. According to Melville and Coleman [27], the coverage diameter of the riprap layer was three times the diameter of the foundation, the thickness of the riprap layer was 2.22, and the propylene was stained in advance for differentiation.

2.2. Test Procedure

Firstly, the sand bed and model were arranged according to the model, as shown in Figure 1a; the soft ruler was set on the model in advance. Then, the rate of the flow was calibrated at a fixed water level by the water level control system. The HD camera placed on the front side of the model was used to capture the phenomenon. In the process

of scour, the destruction process of the riprap protective layer was recorded by an HD camera from multiple positions, the flow pressure on the pile foundation was obtained by a pulsatile pressure sensor, and the topographic data of different scour stages were collected immediately. The topographic data was acquired by a 3D scanner, which can scan terrain and convert it into point cloud data. The same scour terrain was scanned multiple times to obtain multiple groups of point cloud data. MeshLab2022.02 software was used to denoise and repair the point cloud data, and the three-dimensional scour topographic model was reverse established by Geomagic Wrap 2021 and SOLIDWORKS 2022 software. In this test, the velocity data of the pile foundation section and the pressure data of the measuring point were collected and then processed accordingly to verify the accuracy of the numerical model.

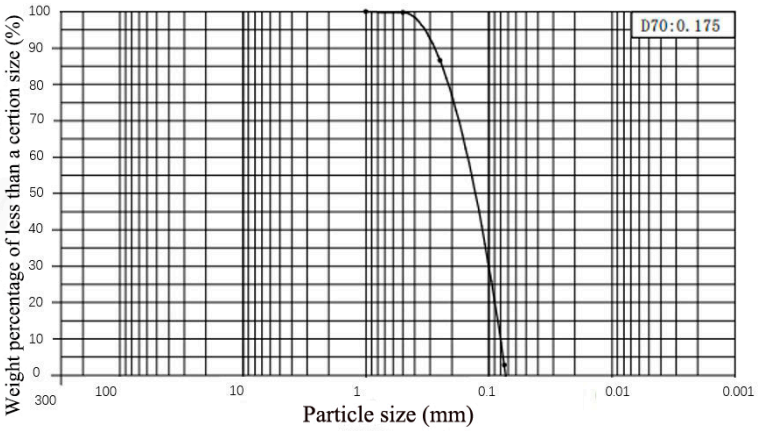

Figure 3. Sediment grading curve.

2.3. Division of Scour Stage

For the visual damage analysis, according to the research results of De Vos et al. [21,22], the riprap damage process can be divided into four stages: in the first stage, no movement of the stones; in the second stage, very limited movement of stones, the outer ring of black riprap cover stone is damaged representing very limited movement of stones; in the third stage, significant movement of stones, the middle ring cover stone is damaged representing significant movement of stones, without failure of the protection; in the fourth stage, the riprap protection fails and forming a stable seabed boundary. The four stages of scour under current are shown in Figure 4.

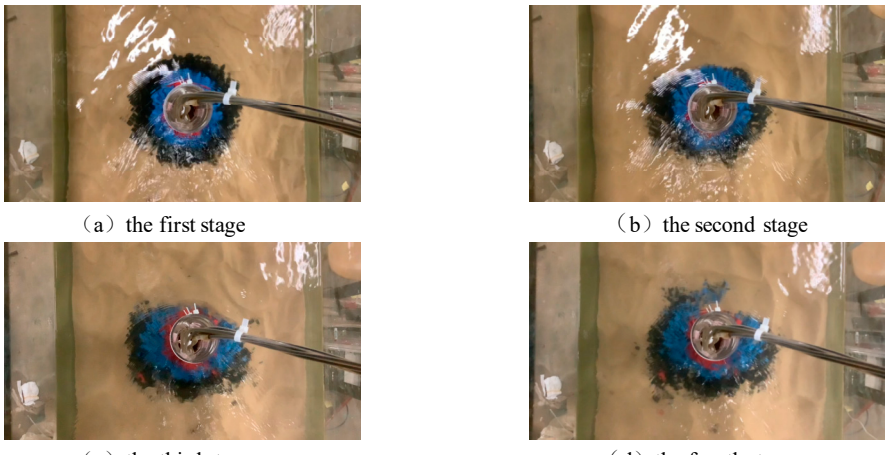

Figure 4. Four stages of scour under current.

3. The Hydrodynamics Numerical Model of Current-Pile-Riprap-Seabed Interaction

Physical model tests are subject to scaling effects and accuracy issues. To study the characteristics in the flow field and pressure field around piles during scour, the CFD method was employed, and a numerical model was established. A three-dimensional numerical model was developed using Flow-3D v11.2 software based on the Navier–Stokes equations and the Renormalization Group (RNG) turbulence model, focusing on the hydrodynamic characteristics of the pile foundation under the influence of current. The numerical solution of the Navier–Stokes equations has been combined with the VOF method to obtain more precise results.

3.1. Numerical Method

3.1.1. Governing Equations

The fluid is regarded as an incompressible viscous Newtonian fluid and is governed by the continuity equation and the Reynolds time-averaged Navier–Stokes equation:

$$\frac{\partial(uA_x)}{\partial x} + \frac{\partial(vA_y)}{\partial y} + \frac{\partial(wA_z)}{\partial z} = 0 \tag{3}$$

The momentum equation is

$$\frac{\partial u}{\partial t} + \frac{1}{V_F}\left(uA_x\frac{\partial u}{\partial x} + vA_y\frac{\partial u}{\partial y} + wA_z\frac{\partial u}{\partial z}\right) = -\frac{1}{\rho}\frac{\partial P}{\partial x} + G_x + f_x \tag{4}$$

$$\frac{\partial v}{\partial t} + \frac{1}{V_F}\left(uA_x\frac{\partial v}{\partial x} + vA_y\frac{\partial v}{\partial y} + wA_z\frac{\partial v}{\partial z}\right) = -\frac{1}{\rho}\frac{\partial P}{\partial y} + G_y + f_y \tag{5}$$

$$\frac{\partial w}{\partial t} + \frac{1}{V_F}\left(uA_x\frac{\partial w}{\partial x} + vA_y\frac{\partial w}{\partial y} + wA_z\frac{\partial w}{\partial z}\right) = -\frac{1}{\rho}\frac{\partial P}{\partial z} + G_z + f_z \tag{6}$$

where ρ is the fluid density; V_F is the volume fraction; $u\ v\ w$ denote the fluid velocity in the $x\ y\ z$ directions; $A_x\ A_y\ A_z$ denote the area fraction in the $x\ y\ z$ directions; $G_x\ G_y\ G_z$ denote body acceleration in the $x\ y\ z$ directions; $f_x\ f_y\ f_z$ denote viscous acceleration in the $x\ y\ z$ directions, respectively.

3.1.2. The Turbulence Model

In the scour test, the water around the pile is violent and chaotic, so the turbulence model was selected in the numerical simulation. Since our study places particular emphasis on vortex dynamics that significantly affect scour outcomes, the renormalization RNG k-ε model was chosen in this paper. This model is derived from a rigorous mathematical treatment of the Navier–Stokes equations, resulting in a modified k-ε formulation that handles high strain rates and near-wall effects effectively. It provides highly accurate predictions for highly swirling flows and curved flows. Its expression is as follows:

$$\frac{\partial k}{\partial t} + \frac{1}{V_F}\left(uA_x\frac{\partial k}{\partial x} + vA_y\frac{\partial k}{\partial y} + wA_z\frac{\partial k}{\partial z}\right) = P + G + D_k - \varepsilon \tag{7}$$

$$\frac{\partial \varepsilon}{\partial t} + \frac{1}{V_F}\left(uA_x\frac{\partial \varepsilon}{\partial x} + vA_y\frac{\partial \varepsilon}{\partial y} + wA_z\frac{\partial \varepsilon}{\partial z}\right) = \frac{C_{1\varepsilon}\cdot\varepsilon}{k}(P + C_{3\varepsilon}\cdot G) + D_\varepsilon - C_{2\varepsilon}\frac{\varepsilon^2}{k} \tag{8}$$

where G is the turbulent kinetic energy generation term; its value is 0. P is the kinetic energy generation term generated by the velocity gradient, k is the turbulent kinetic energy.

3.1.3. Boundary Conditions and the Initial Conditions

For the numerical flume in this paper, the X_{min} section was set to Specified velocity, the X_{max} section was set to Specified pressure, three sections were set to Symmetry, including Y_{min}, Y_{max}, and Z_{max}, and the section of Z_{min} was set to Wall. The water depth was 0.15 m, and the flow velocity was 0.387 m/s. Other conditions and parameters in the numerical model were consistent with the experimental conditions, and the initial conditions were set by giving the flow field characteristics of the water in the mesh computational domain.

3.2. Establishment and Verification of the Numerical Model

3.2.1. Establishment of Numerical Model

The parameters of the numerical flume computational domain were set based on the physical model experimental conditions. The 3D topographic data were utilized to establish a 3D scour topographic model. A mesh computational domain, Mesh block1, with dimensions of 15 m × 0.6 m × 0.25 m, was established with a mesh size of 0.01 m. Since the flow velocity on the boundaries set by FLOW-3D is uniform along the vertical section, which differs from the actual flow velocity distribution in the fluid, a flow development region must be defined to ensure stable fluid development. According to Kirkgoz et al. [28], the pile foundation was placed in the flume after a 9.59 m position to ensure the same flow conditions as the experiment.

The area surrounding the pile foundation was discretized separately using mesh blocks, with Mesh Block2 for densification. Mesh sizes of 0.01 m, 0.005 m, and 0.0025 m were chosen for Mesh Block2, yielding uniform meshes, as shown in Figure 5. The specific mesh quantities, sizes, and computational times are shown in Table 3. The mesh parameters of the numerical flume are shown in Table 4. Employing the FAVOR (Fractional Area/Volume Obstacle Representation) technique, the acquired topographic data model was processed, as depicted in Figure 6. Considering the resultant shape of the model after FAVOR processing, the proportionality of adjacent mesh blocks, and computational efficiency and accuracy, a mesh size of 0.005 m was selected for the densification of the area surrounding the pile foundation.

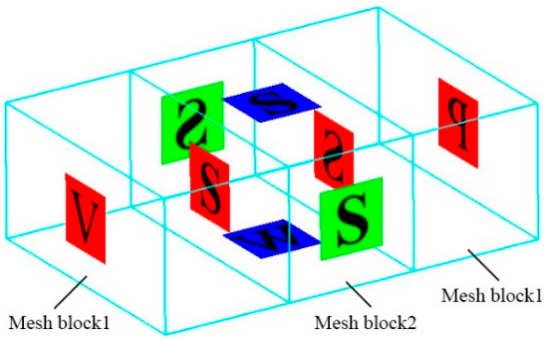

Figure 5. Meshblock1 and Meshblock2 in the numerical model.

Table 3. Mesh size and quantity of Mesh block2.

Mesh Size (m)	Mesh Quantity (Million)	Δ*x* (m)	Δ*y* (m)	Δ*z* (m)	Computational Times (min)
0.01	0.3	0.01	0.01	0.01	240
0.005	2.4	0.005	0.005	0.005	480
0.0025	19.2	0.0025	0.0025	0.0025	1260

Table 4. Mesh parameters of the numerical flume.

	Domain Size (m^3)	Mesh Size (m)	Mesh Quantity (Million)
Mesh block1	15 × 0.6 × 0.25	0.01	2.25
Mesh block2	2 × 0.6 × 0.25	0.005	2.4

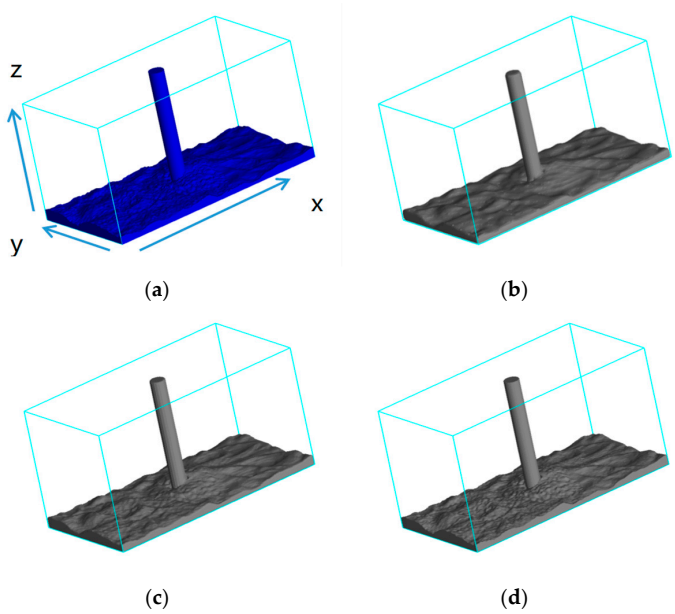

Figure 6. Comparison of different grid sizes in Mesh block2. (**a**) Unprocessed model. (**b**) FAVOR processed (0.01 m). (**c**) FAVOR processed (0.005 m). (**d**) FAVOR processed (0.0025 m).

3.2.2. Verification of Numerical Model

The data of Roulund et al. [29] was selected as a comparison, and the comparison between the experimental flume's velocity section data and the numerical simulation results is shown in Figure 7. The velocities were sampled at three different depths from the bed: z = 0.005 m, 0.01 m, and 0.02 m. The horizontal velocity u comparison is shown in Figure 8a, and the vertical velocity w comparison is shown in Figure 8b. It can be seen that the numerical simulation results of horizontal and vertical flow velocity distribution at different water depths are in good agreement with the data of Roulund et al. [29], indicating the reliability of the numerical model.

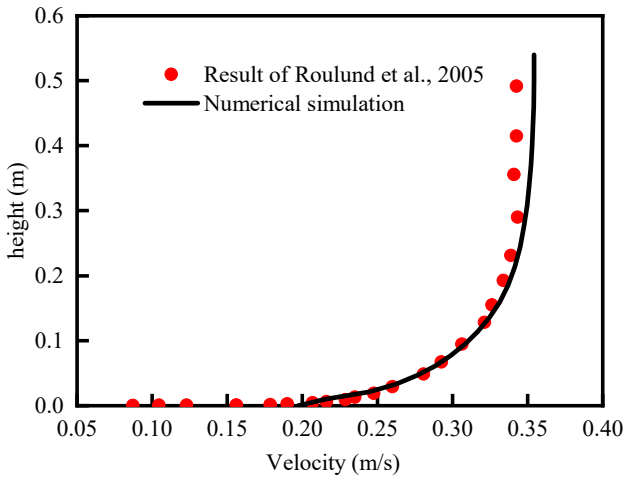

Figure 7. Comparison of cross-section flow velocity distribution [29].

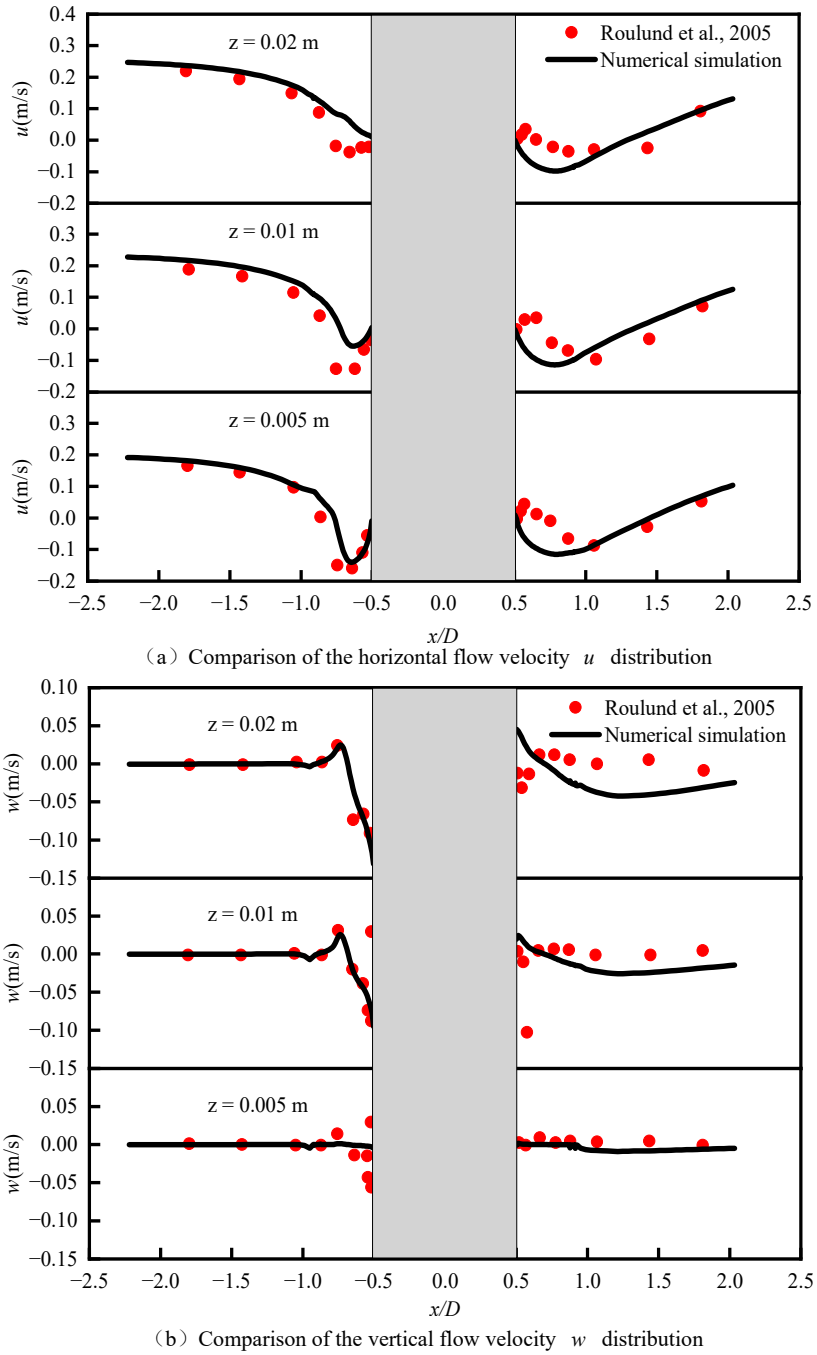

（a）Comparison of the horizontal flow velocity u distribution

（b）Comparison of the vertical flow velocity w distribution

Figure 8. Comparison of the flow velocity around the pile [29].

Five virtual pressure measurement points, labeled as P1 to P5, were arranged on the front side and back side of the pile foundation, following the same layout as shown in experimental Figure 2. The pressure data under the current conditions are dimensionless, and the non-dimensional parameter η, defined as the ratio of the impulsive pressure p_c to the hydrostatic pressure at the position of the measurement point was used for characterization:

$$\eta = \frac{p_c}{\rho g y} \tag{9}$$

where ρ is the fluid density; g is the gravitational acceleration, 9.8 m/s^2.

Figure 9a–d shows the comparison diagram of dimensionless pressure parameter test results and numerical simulation results at measuring points P1 to P5 in four stages of 0.15

m, flow velocity of 0.387 m/s, and riprap protection under the action of current. It can be seen that the data from the experiment and numerical simulation agree well, proving the accuracy of the numerical model.

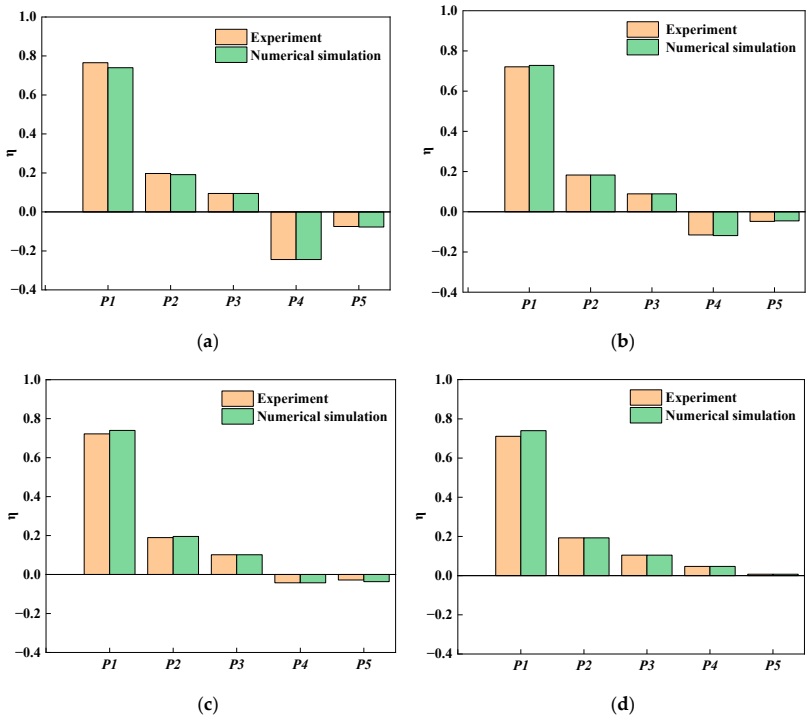

Figure 9. Comparison of dimensionless pressure parameter η from *P1* to *P5*. (**a**) The first stage. (**b**) The second stage. (**c**) The third stage. (**d**) The fourth stage.

4. Hydrodynamic Characteristics Around the Pile Foundation

4.1. Characteristics of the Flow Field Around the Pile Foundation

The profiles of the *X*-*Z* section (*Y* = 0 m), *Y*-*Z* section (θ = 0°, 45°, 90°, 135°, 180°), and *X*-*Y* section (*Z* = 0.5*D*, *D*, 1.5*D*, 2*D*) based on the numerical simulation model are shown in Figure 10.

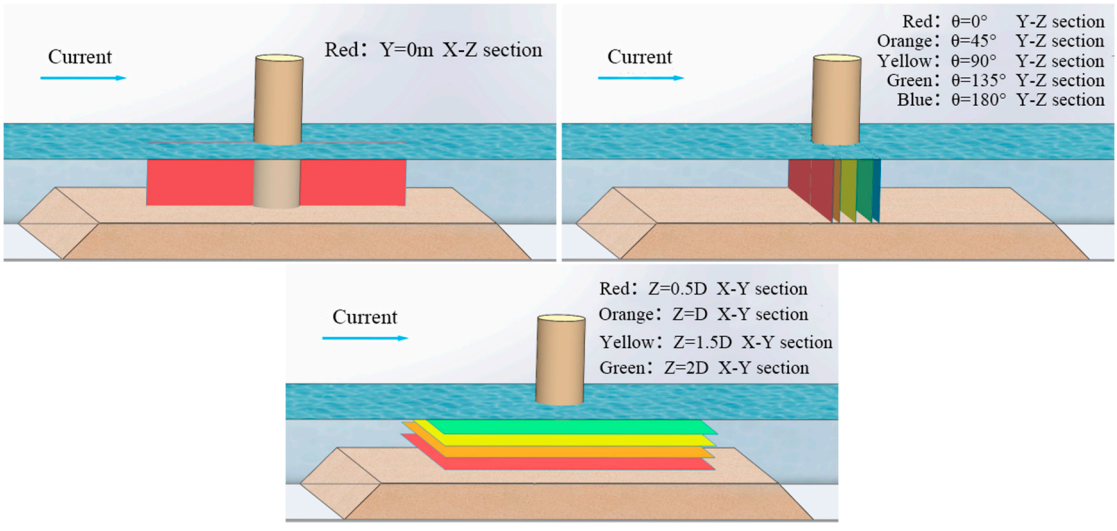

Figure 10. Flow field section.

4.1.1. Velocity of *X*-*Z* Section

The velocity contour maps and velocity vector maps of the *X*-*Z* section at different scour stages are shown in Figure 11. Through comparative analysis, it is found that the maximum flow velocity of the section gradually decreases from the first stage to the fourth stage.

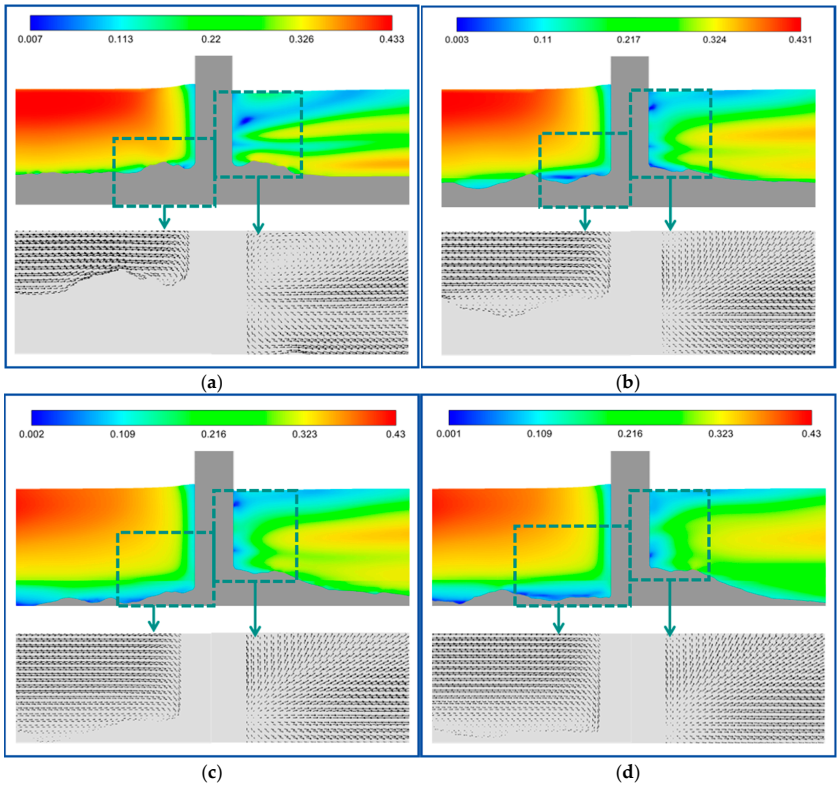

Figure 11. Velocity contour and velocity vector of the *X*-*Z* section at different scour stages. (**a**) The first stage. (**b**) The second stage. (**c**) The third stage. (**d**) The fourth stage.

According to Figure 11, it can be observed that the flow is obstructed by the pile foundation, resulting in a reduced flow velocity in front of the pile and the generation of a downward flow. In velocity contour maps of Figure 11b–d, there exists a small area A1 with an almost zero flow velocity in front of the riprap protection. It is evident that, as scour progresses, the low velocity region in front of the pile near the seabed expands. At the onset of scour, the presence of riprap restricts the formation of this low velocity zone, resulting in a higher minimum velocity in the region compared to the steady state scour condition. The velocity vector maps of Figure 11b–d illustrate that there are small vortices present in this area, which effectively weaken the kinetic energy of the downward flow and reduce the scour effect of the flow on the front side of the pile foundation.

Similarly, there are small regions B1 and B2 at the back of the pile near the riprap protection layer where the flow velocity is nearly zero. In the velocity vector maps of Figure 11b–d, it can be observed that small vortices exist within area B1. These vortices are generated due to the disturbance created by the flow passing in front of the pile foundation, resulting in upward flow after interacting with the riprap protection. The vector maps in Figure 11b–d indicate that in area B2, there are flow velocities directed both upwards and downwards. The upward flow converges into the low velocity area B1, while the downward flow moves toward the back riprap protection of the pile. As the scour phase progresses, the small, low-velocity area B1 gradually decreases in size, with its height rising closer to the water surface, while the shape and elevation of the small low-velocity area

B2 remain relatively unchanged. The presence of the small, low-velocity area B2 effectively facilitates the deposition of sediment carried by the advancing flow, allowing it to settle near the back riprap protection of the pile.

4.1.2. Velocity of *Y-Z* Section

Figure 12 shows velocity contours of the *Y-Z* section at different θ angles under the scour of the current. Figures 13–17 show the velocity contours at different scour stages from various θ angles of the riprap-protected monopile. Combined with Figures 12–17, it can be seen that when the flow passes through unprotected pile foundation and riprap-protected pile foundation, the maximum flow velocity of the section shows a trend of first increases (from 0° to 90°) and then decreases (from 90° to 180°), reaching its maximum when θ = 90° (center of the pile foundation). The comparison of Figures 12 and 13a–17a shows that the decrease in water depth in front of the pile, caused by riprap protection, results in a reduction of the overflow area, leading to an increase in flow velocity. Consequently, the maximum flow velocity increases by 6.04%, 5.63%, 7.23%, 3.48% and 4.62% within θ from 0° to 180°, respectively. In the fourth stage of scour, the pile foundation protected by riprap reduces the distribution of the maximum flow velocity in the range of θ = 0–180° by 11.46%, 12.12%, 9.32%, 16.72%, and 17.05%, respectively.

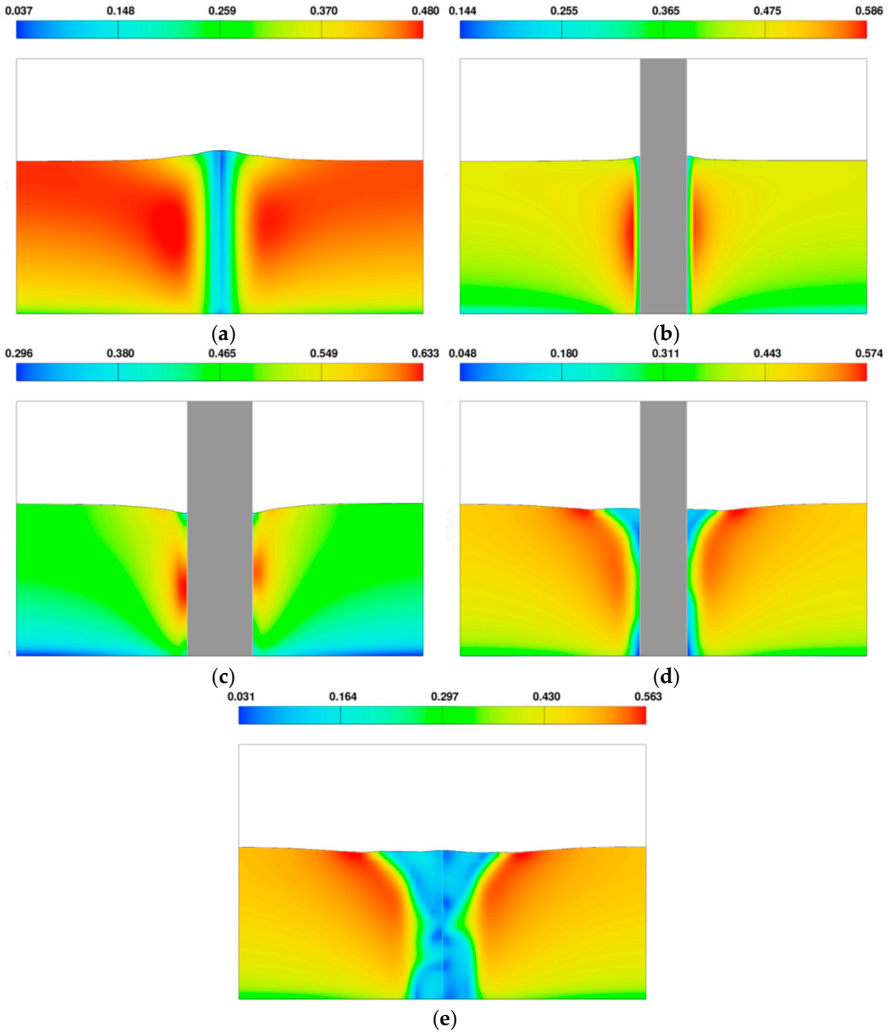

Figure 12. *Y-Z* section velocity contour of unprotected pile foundation at different θ angles. (**a**) 0° *Y-Z* section velocity contour. (**b**) 45° *Y-Z* section velocity contour. (**c**) 90° *Y-Z* section velocity contour. (**d**) 135° *Y-Z* section velocity contour. (**e**) 180° *Y-Z* section velocity contour.

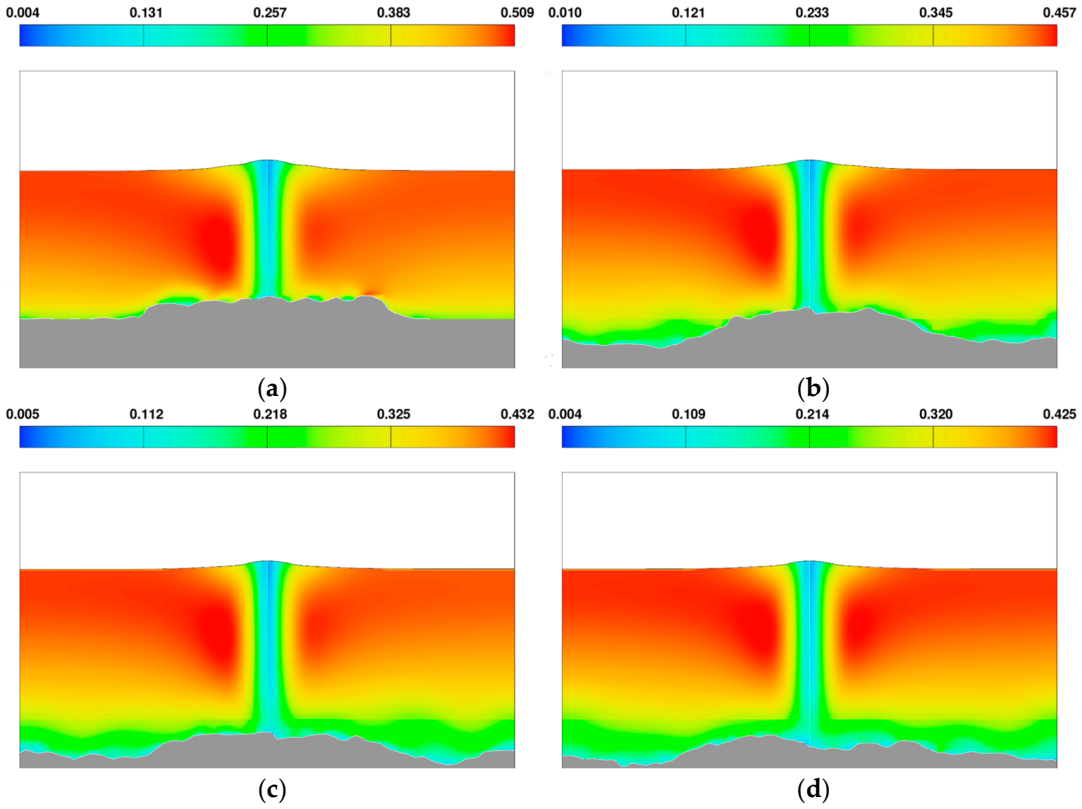

Figure 13. *Y-Z* section velocity contour of protected pile foundation at $\theta = 0°$. (**a**) The first stage. (**b**) The second stage. (**c**) The third stage. (**d**) The fourth stage.

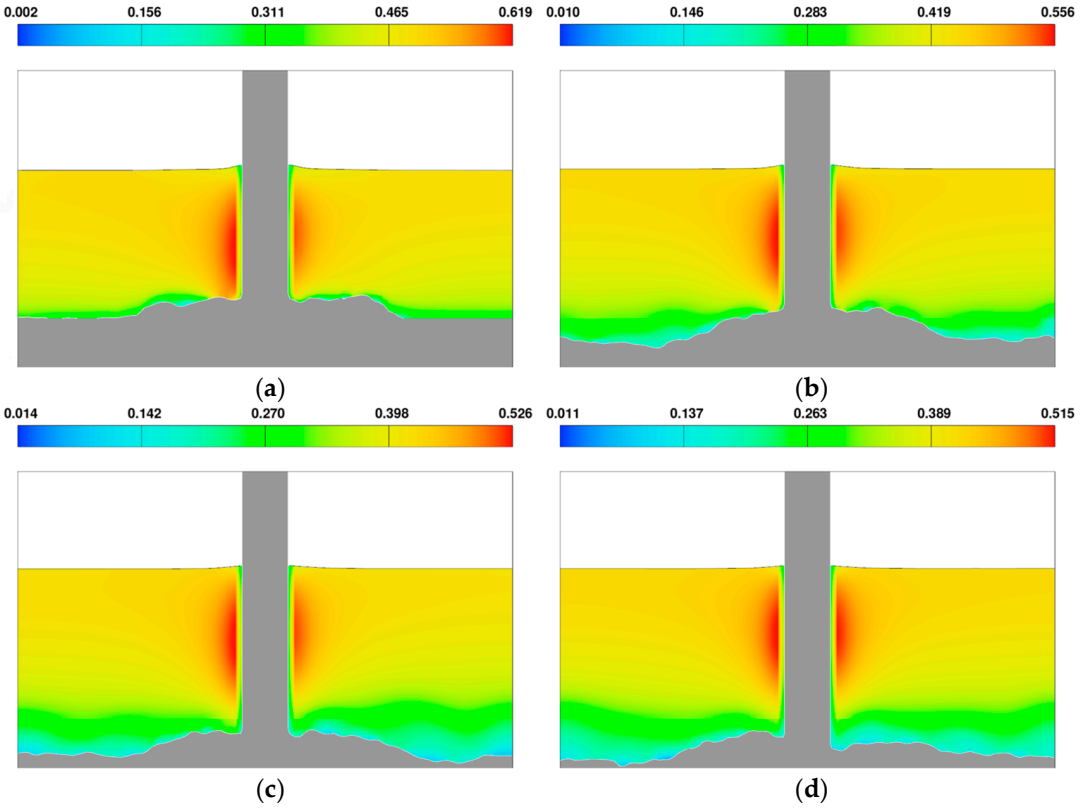

Figure 14. *Y-Z* section velocity contour of protected pile foundation at $\theta = 45°$. (**a**) The first stage. (**b**) The second stage. (**c**) The third stage. (**d**) The fourth stage.

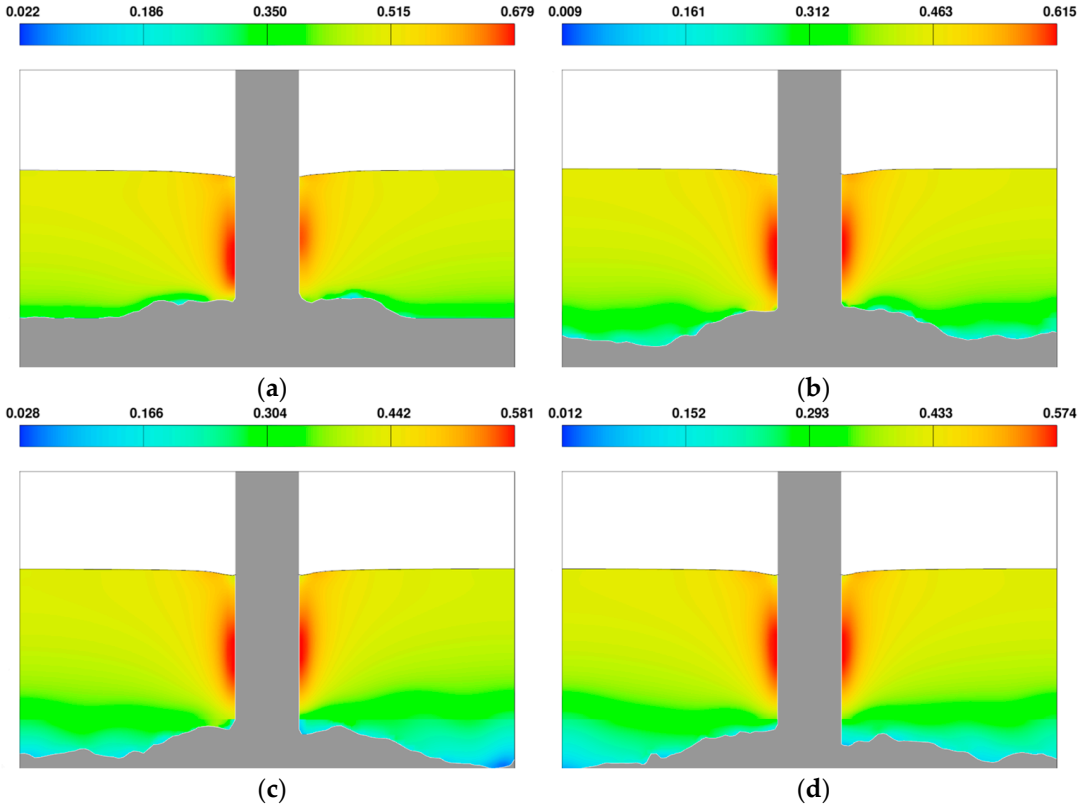

Figure 15. *Y-Z* section velocity contour of protected pile foundation at $\theta = 90°$. (**a**) The first stage. (**b**) The second stage. (**c**) The third stage. (**d**) The fourth stage.

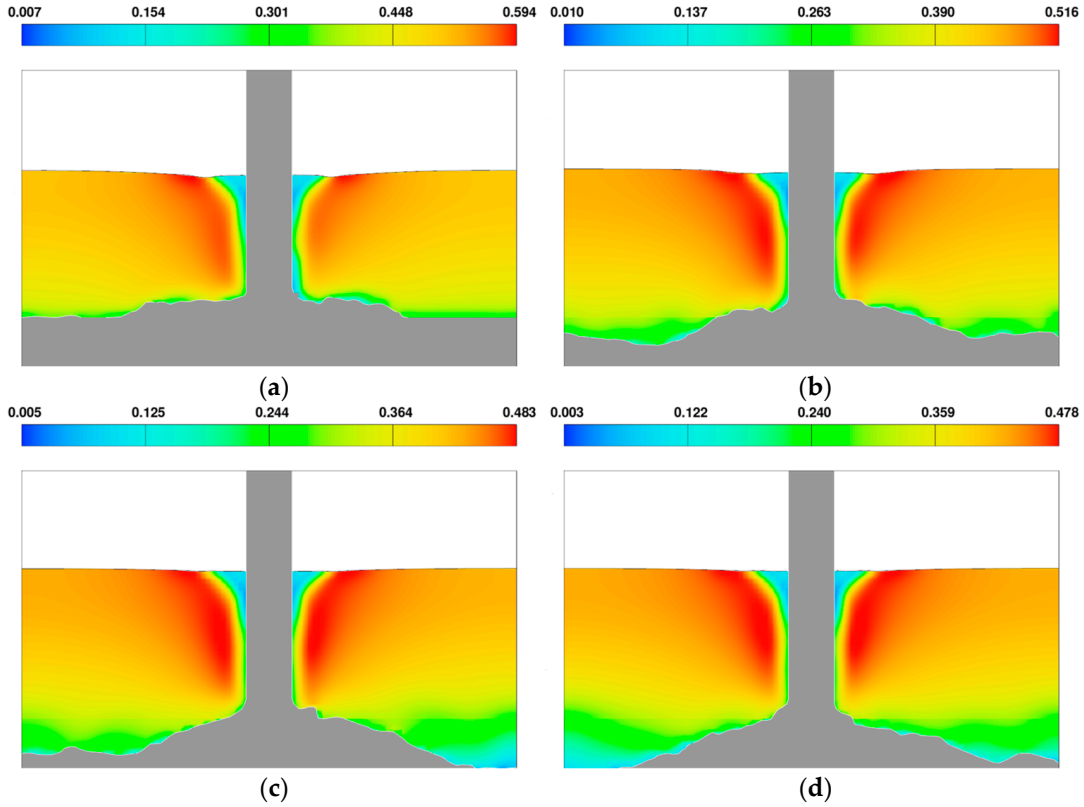

Figure 16. *Y-Z* section velocity contour of protected pile foundation at $\theta = 135°$. (**a**) The first stage. (**b**) The second stage. (**c**) The third stage. (**d**) The fourth stage.

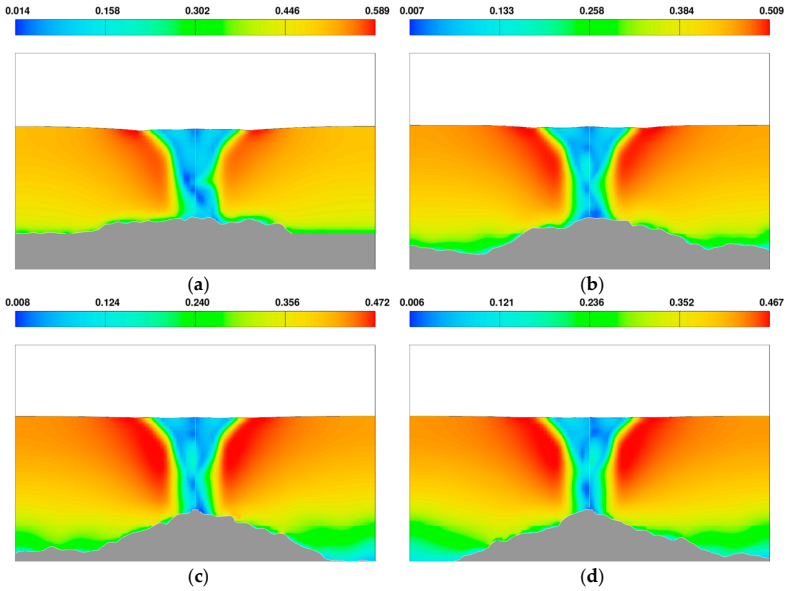

Figure 17. *Y*-*Z* section velocity contour of protected pile foundation at $\theta = 180°$. (**a**) The first stage. (**b**) The second stage. (**c**) The third stage. (**d**) The fourth stage.

4.1.3. Velocity of *X*-*Y* Section

Figure 18 shows velocity contours of the *X*-*Y* section at different elevations *Z* under the scour of the current, where *Z* represents the vertical distance between the *X*-*Y* section to be observed and the seabed surface. Figures 19–22 show the flow velocity contours of the *X*-*Y* section at different elevations *Z* of the riprap-protected monopile. On the whole, at the same scour stage, as *Z* increases and the section moves farther away from the bed surface, the maximum flow velocity around both sides of the pile foundation showed a trend of increasing first (from 0.5*D* to *D*) and then decreasing (from *D* to 2*D*). The minimum flow velocity occurs at the back of the pile foundation, reaching its maximum range at the elevation $Z = 2D$, which is consistent with the observations in Figure 11. Comparing Figures 18, 19a–22a, it can be seen that due to the formation of the riprap protection, the maximum flow velocity increased by 6.53%, 4.62%, 2.54%, and 3.42% in the range of $Z = 0.5D$–$2D$, respectively. In the fourth stage of scour, the maximum flow velocity around the protected pile foundation was reduced by 12.39%, 12.48%, 11.78%, and 10.79%, respectively, in the range of $Z = 0.5D$–$2D$.

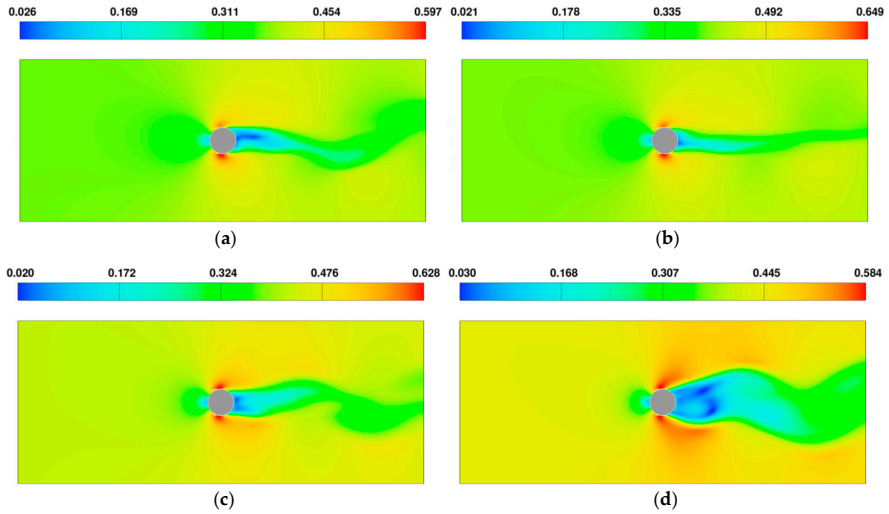

Figure 18. *X*-*Y* section velocity contour of unprotected pile foundation at different *Z*. (**a**) $Z = 0.5D$. (**b**) $Z = D$. (**c**) $Z = 0.75D$. (**d**) $Z = 2D$.

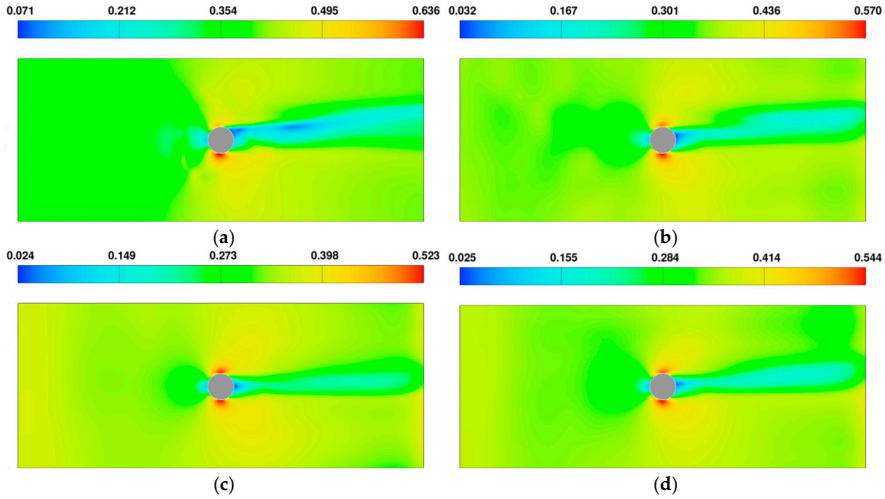

Figure 19. *X-Y* section velocity contour of protected pile foundation at $Z = 0.5D$. (**a**) The first stage. (**b**) The second stage. (**c**) The third stage. (**d**) The fourth stage.

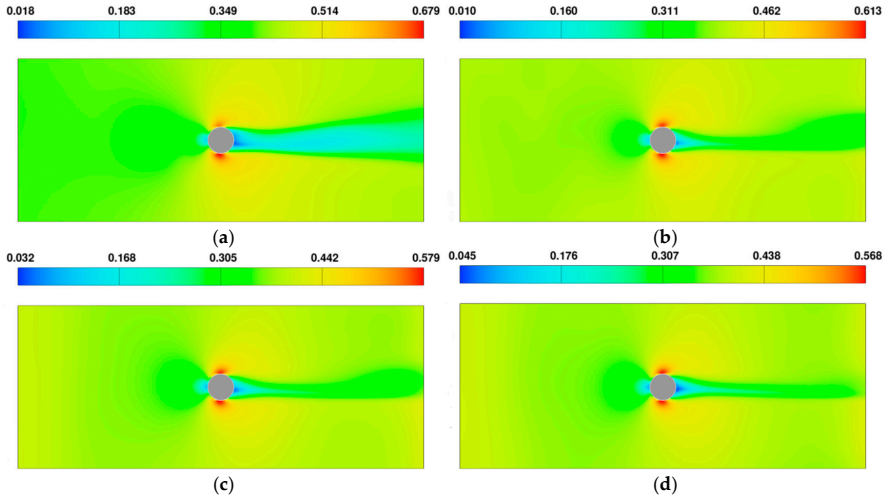

Figure 20. *X-Y* section velocity contour of protected pile foundation at $Z = D$. (**a**) The first stage. (**b**) The second stage. (**c**) The third stage. (**d**) The fourth stage.

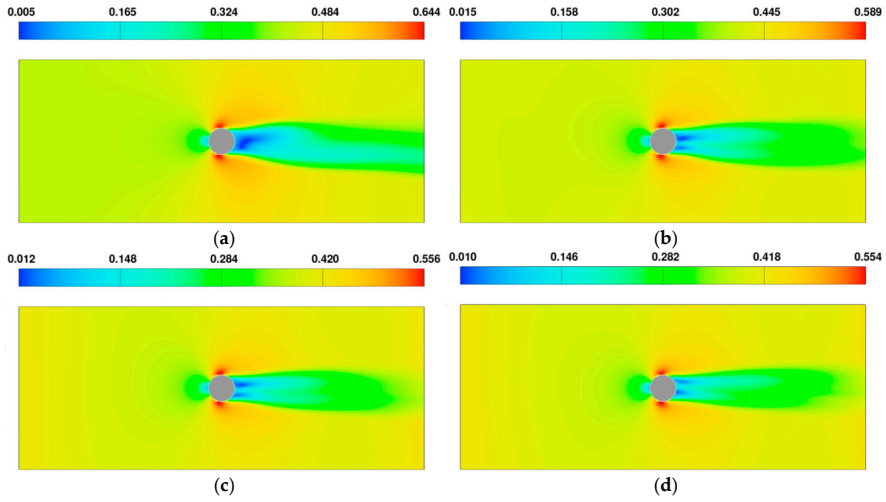

Figure 21. *X-Y* section velocity contour of protected pile foundation at $Z = 1.5D$. (**a**) The first stage. (**b**) The second stage. (**c**) The third stage. (**d**) The fourth stage.

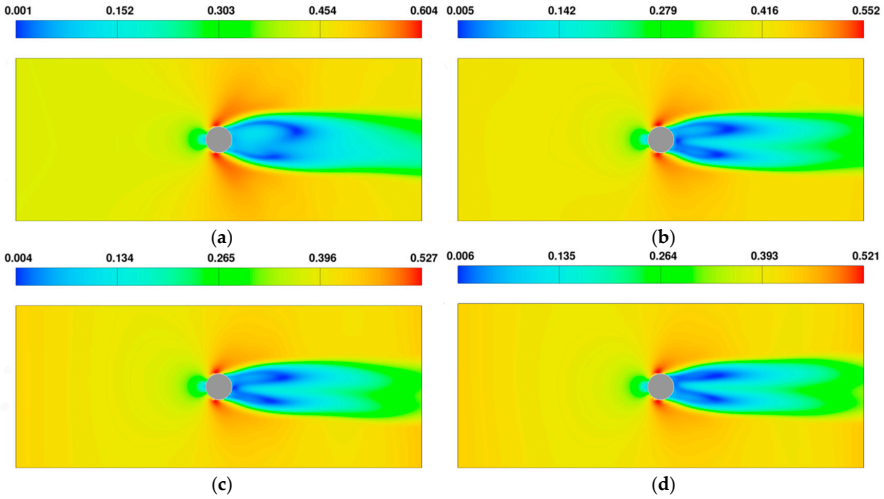

Figure 22. *X-Y* section velocity contour of protected pile foundation at $Z = 2D$. (**a**) The first stage. (**b**) The second stage. (**c**) The third stage. (**d**) The fourth stage.

4.2. Horseshoe Vortex

In order to show the position and strength of the horseshoe vortex before the pile foundation, the Q criterion [30] was used to identify the vortex. The expression formula of the Q criterion is as follows:

$$Q = \frac{1}{2}\left(\|B\|_F^2 - \|A\|_F^2\right) = -\frac{1}{2}\left[\left(\frac{\partial u}{\partial x}\right)^2 + \left(\frac{\partial v}{\partial y}\right)^2 + \left(\frac{\partial w}{\partial z}\right)^2\right) + 2\frac{\partial u}{\partial y}\frac{\partial v}{\partial x} + 2\frac{\partial u}{\partial z}\frac{\partial w}{\partial x} + 2\frac{\partial v}{\partial z}\frac{\partial w}{\partial y}\Bigg] \tag{10}$$

where B denotes the antisymmetric part of the velocity gradient tensor in the flow field, while A represents the symmetric part, corresponding to deformation and rotation in the flow field, respectively. When the Q value is greater than 0, the displayed region indicates the location of vortices, where the rotational intensity in the flow field predominates over deformation.

Figure 23 presents the three-dimensional vortex structure around the cylinder of an unprotected pile foundation under the action of current with a water depth of 0.15 m, a flow velocity of 0.387 m/s, and a circulation number Q of 5. Figure 24 illustrates the three-dimensional vortex structures surrounding the cylinder at various scour stages under identical flow conditions, with riprap protection measures ($Q = 5$). By comparing Figures 23a and 24a, it can be observed that the presence of riprap protection in front of the pile results in a significantly larger range of vortices above the riprap protection.

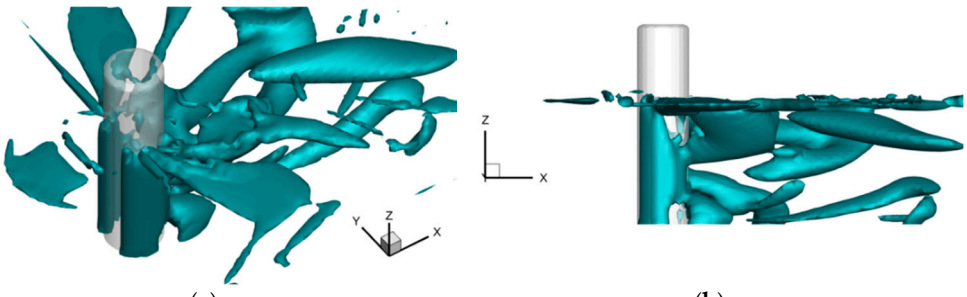

Figure 23. Three-dimensional vortex structure around the unprotected cylinder ($Q = 5$). (**a**) Three-dimensional graph. (**b**) Side view.

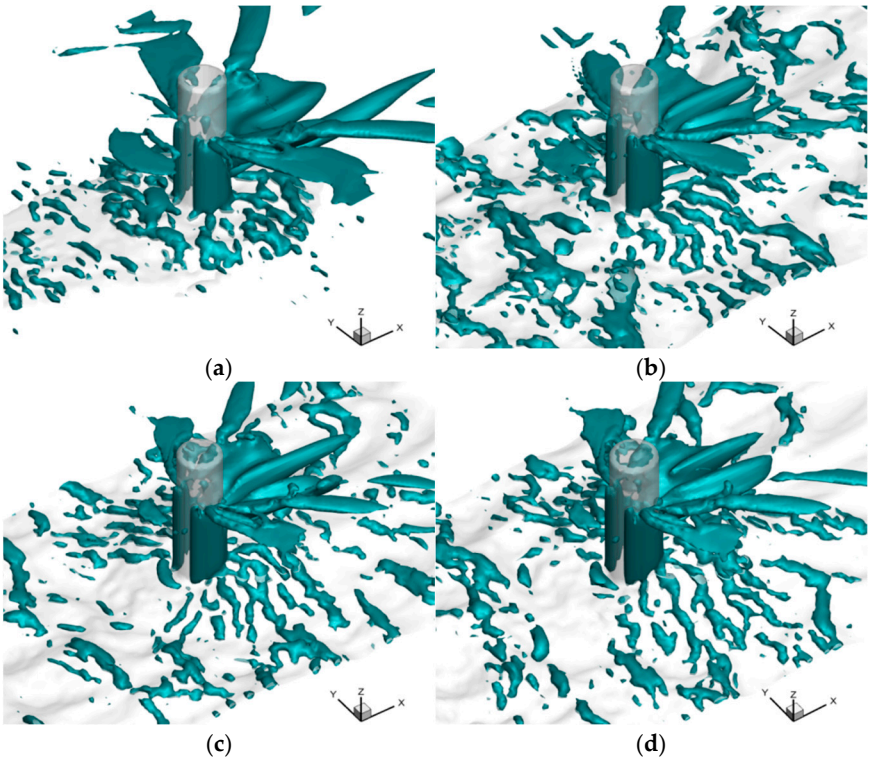

Figure 24. Three-dimensional vortex structure around the cylinder with riprap protection (Q = 5). (**a**) The first stage. (**b**) The second stage. (**c**) The third stage. (**d**) The fourth stage.

Comparing Figure 24a–d, it can be seen that after implementing riprap protection measures for the pile foundation, the range of vortices in front of the pile gradually decreases, and their shapes tend toward stability. Through an overall analysis combining Figures 23a and 24, it is evident that the presence of riprap protection in front of the pile leads to a reduction in water height in front of the pile, enhancing the intensity of downward flow above the riprap protection. This results in the formation of larger horseshoe vortices in front of the pile. As scour progresses, the depth of scour in front of the pile tends to stabilize, leading to a gradual reduction in the range of the horseshoe vortices, with their shapes approaching stability.

The evolution of the horseshoe vortices in front of the pile, transitioning from no protection to riprap protection and then to the last scour stage, exhibits a trend of initially increasing and then decreasing in range. This trend aligns with the findings of Muzzammil and Gangadliariali [31] regarding the evolution of horseshoe vortices in monopile scour without protective measures.

4.3. Wake Vortex

Figure 25 presents the three-dimensional vortex structure behind the cylindrical pile foundation with rock protection under the action of current, with a water depth of 0.15 m and a flow velocity of 0.387 m/s, during different scour stages (Q = 5). Combining Figures 23–25, it can be observed that the wake vortex behind the pile is mainly composed of three parts: the vortex field near the water surface on both sides of the pile, the vortex field near the water surface behind the pile, and the vortex field near the seabed surface behind the pile. Comparing Figures 23 and 25a, it can be seen that before implementing rock protection, there is significant shedding of vortices behind the pile in the direction of flow. After implementing riprap protection around the pile, the vortex field near the water surface on both sides of the pile remains relatively unchanged, while changes occur in the vortex field behind the pile near the water surface. The phenomenon of rotational shedding

no longer occurs behind the pile, and the vortex near the riprap protection behind the pile forms a coarse and elongated shape. According to Figure 11, the reason for the changes in the vortex field after implementing riprap protection around the pile is that the flow disturbance and lift caused by the pile and riprap protection affect the formation of vortices above the riprap protection behind the pile. Comparing Figure 25a–d, as scour progresses, the shape and size of the wake vortex near the water surface remain basically unchanged, while the wake vortex near the riprap protection gradually becomes thinner and shorter, disappearing completely in the stable fourth stage of scour.

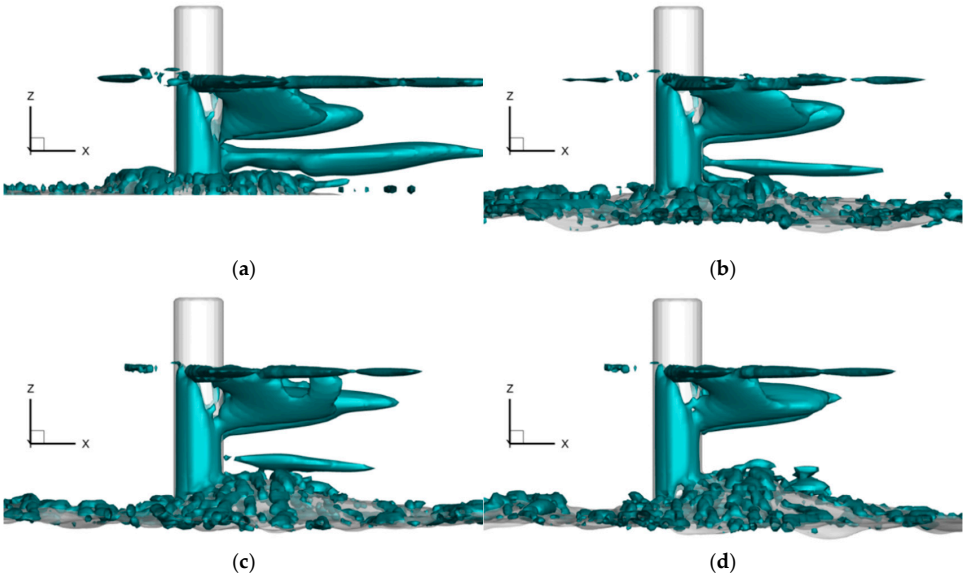

Figure 25. Three-dimensional vortex structure around the cylinder with riprap protection (Q = 5). (**a**) The first stage. (**b**) The second stage. (**c**) The third stage. (**d**) The fourth stage.

4.4. Pressure Distribution Around the Pile Foundation

According to symmetry, only one side of the pile foundation was selected for study. Five columns of pressure sensors were evenly arranged at intervals of 45° within the range of θ = 0–180° on the side of the pile foundation. These columns were labeled as Row A, Row B, Row C, Row D, and Row E. Along the elevation direction, four pressure observation points were arranged at intervals of 0.5D for each column of sensors, where Z is defined as the vertical distance from the data recording point to the seabed surface. The specific arrangement of data recording points is shown in Figure 26 and Tables 5 and 6.

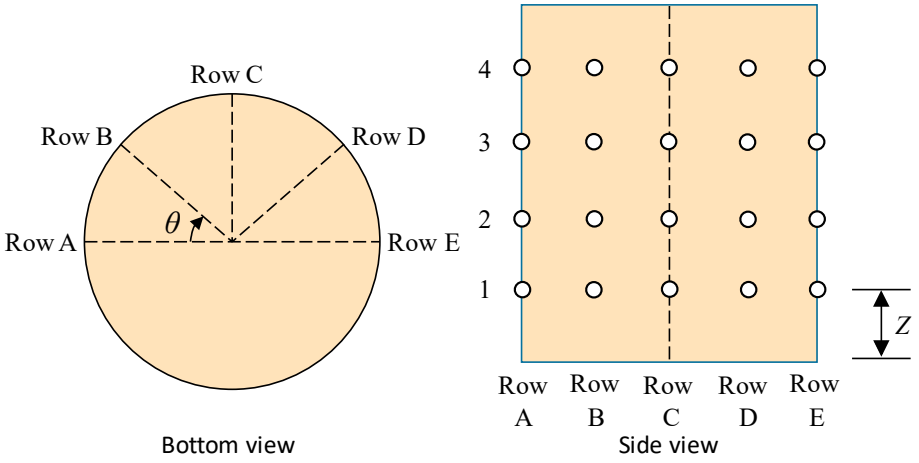

Figure 26. Pressure observation point setting.

Table 5. Location of pressure observation point on the pile at different heights.

Z/*D*	Row A	Row B	Row C	Row D	Row E
0.5	A1	B1	C1	D1	E1
1	A2	B2	C2	D2	E2
1.5	A3	B3	C3	D3	E3
2	A4	B4	C4	D4	E4

Table 6. Location of pressure observation point on pile in different θ.

θ (°)	Observation Point
0	A1–A4
45	B1–B4
90	C1–C4
135	D1–D4
180	E1–E4

Figures 27–31 show the comparison diagram of the numerical simulation results of the pressure parameters of each pressure measurement point from Row A to Row E, L represents the unprotected pile foundation, and L1 to L4 correspond to the four scour stages, respectively.

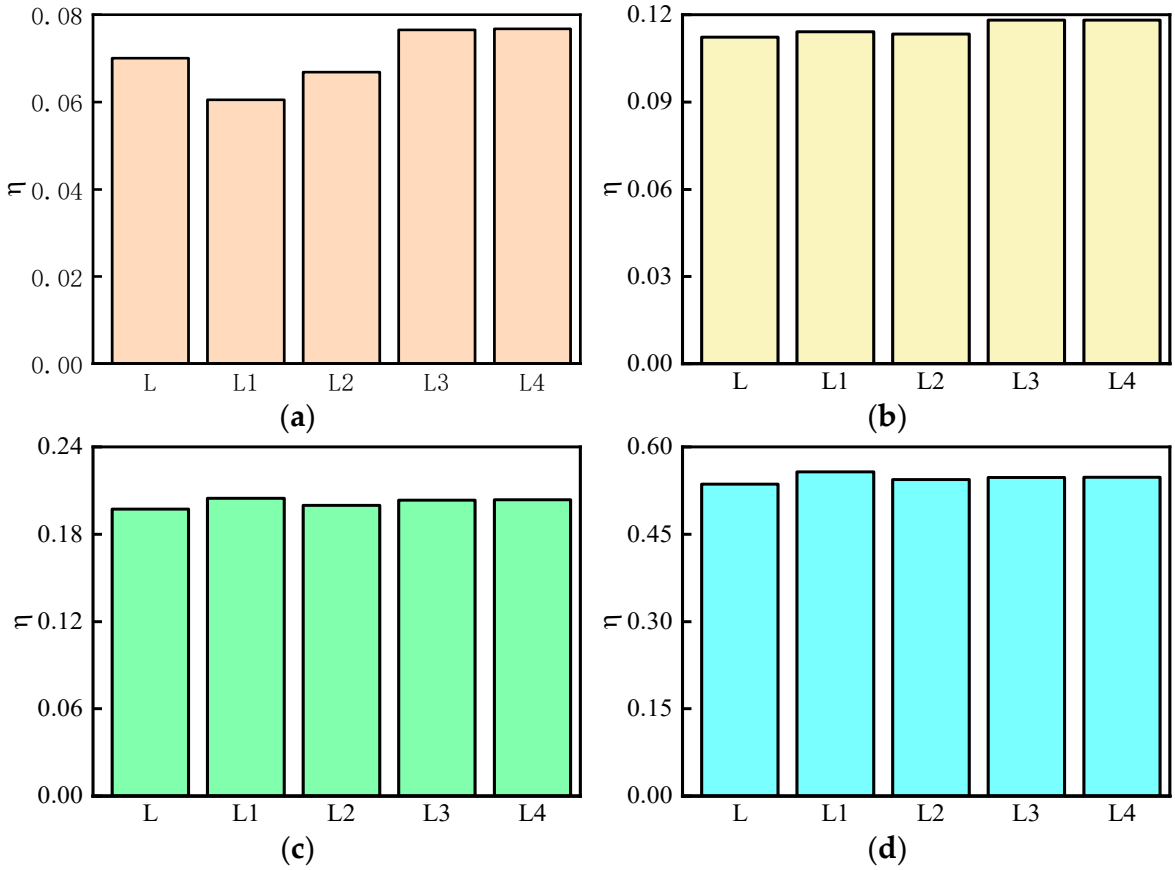

Figure 27. Numerical simulation of the pressure parameter η from the measurement point A1 to A4. (**a**) measurement point A1. (**b**) Measurement point A2. (**c**) Measurement point A3. (**d**) Measurement point A4.

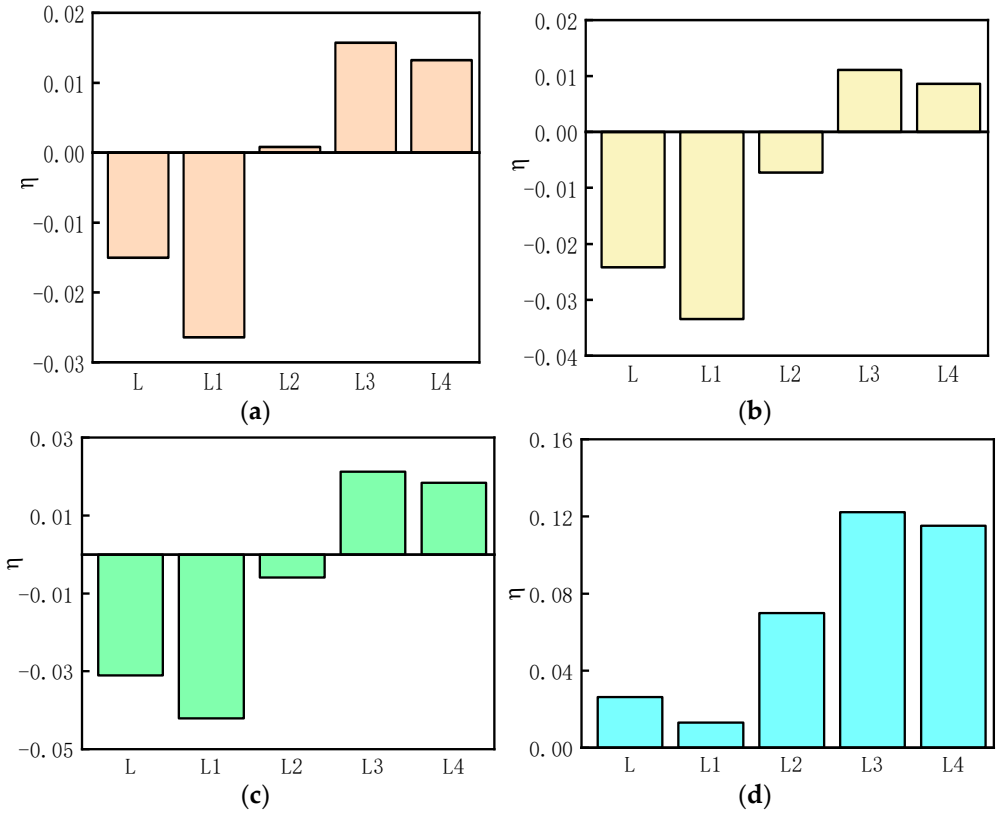

Figure 28. Numerical simulation of the pressure parameter η from the measurement point B1 to B4. (**a**) Measurement point B1. (**b**) Measurement point B2. (**c**) Measurement point B3. (**d**) Measurement point B4.

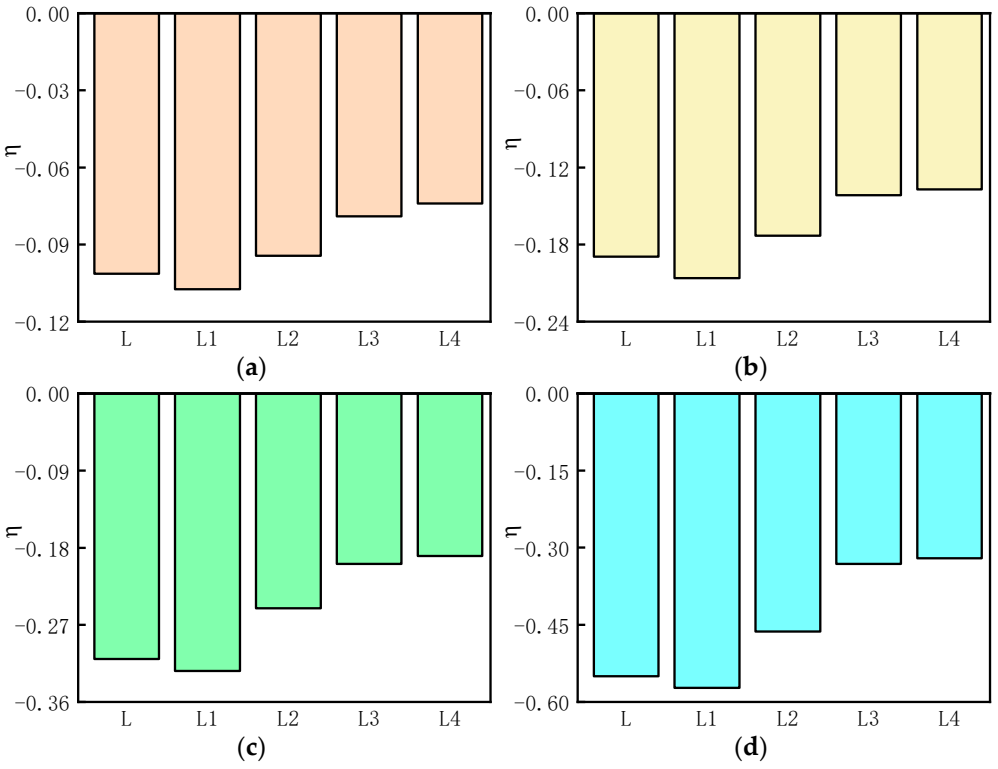

Figure 29. Numerical simulation of the pressure parameter η from the measurement point C1 to C4. (**a**) Measurement point C1. (**b**) Measurement point C2. (**c**) Measurement point C3. (**d**) Measurement point C4.

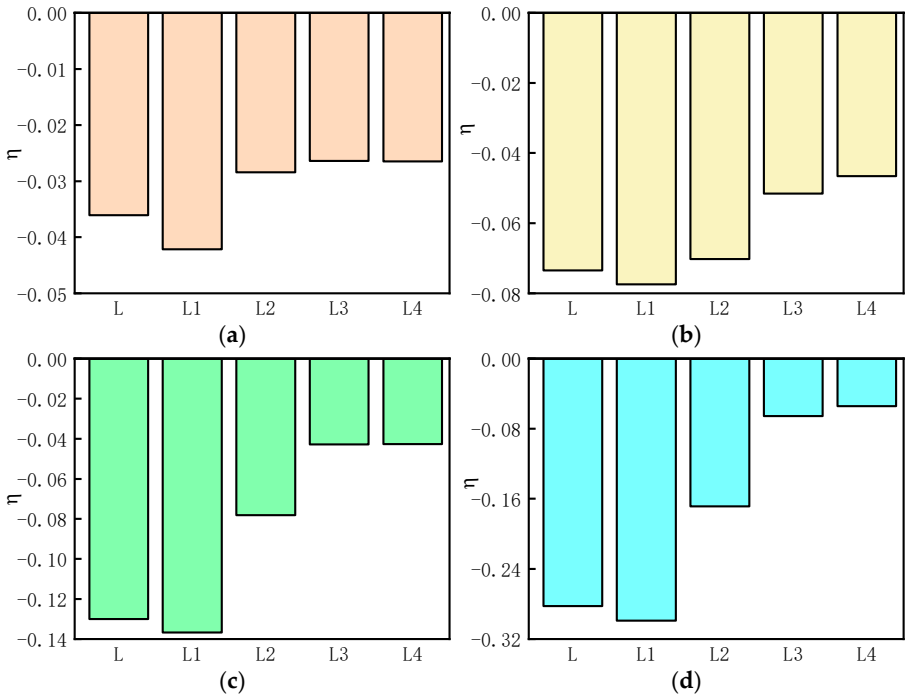

Figure 30. Numerical simulation of the pressure parameter η from the measurement point D1 to D4. (**a**) Measurement point D1. (**b**) Measurement point D2. (**c**) Measurement point D3. (**d**) Measurement point D4.

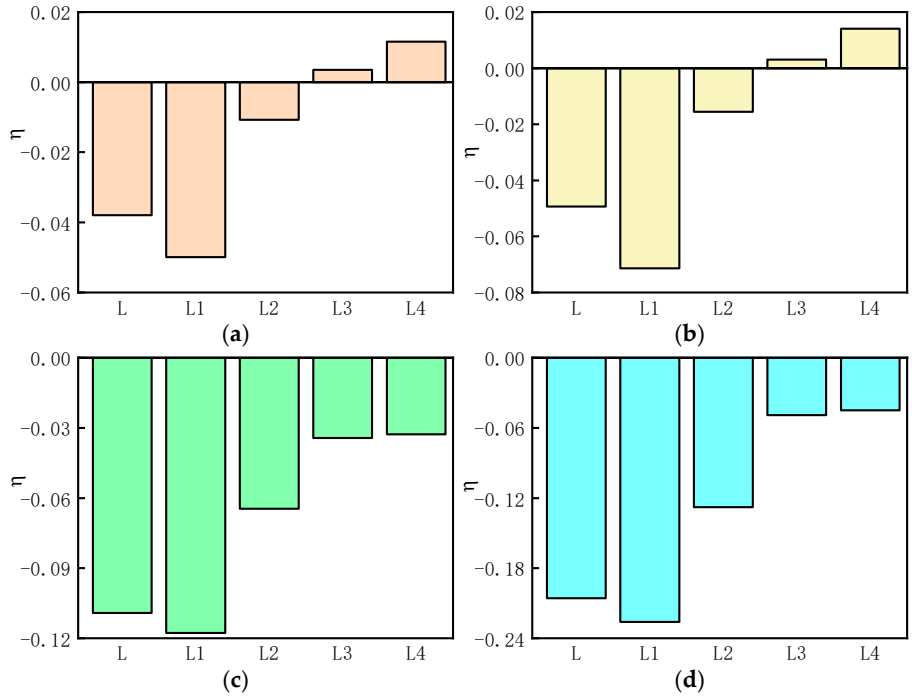

Figure 31. Numerical simulation of the pressure parameter η from the measurement point E1 to E4. (**a**) Measurement point E1. (**b**) Measurement point E2. (**c**) Measurement point E3. (**d**) Measurement point E4.

For the same scour stage and different elevation Z, different pressure measurement points within a single column (Row) exhibit an increasing trend in pressure as the elevation Z increases, attributed to the distribution characteristics of cross-sectional flow velocity and the positive correlation between impact pressure and flow velocity. The minimum pressure value occurs at pressure measurement point E4 in Row E during the L1 stage,

with a pressure reduction of 22.61% compared to the static water pressure at that location. The maximum pressure value occurs at pressure measurement point A4 in Row A during the L1 stage, exceeding the static water pressure at that location by 55.73%.

For the same scour stage and same elevation Z, different pressure measurement points at various angles θ exhibit a trend of decreasing pressure (Row A–Row C) followed by an increase (Row C–Row E) due to flow disturbance caused by the obstruction of the pile foundation as the flow passes it. The maximum increase in pressure values is 8.64% ($\theta = 0°$), 338% ($\theta = 45°$), 41.67% ($\theta = 90°$), 80.85% ($\theta = 135°$), and 131% ($\theta = 180°$).

5. Conclusions

The hydrodynamic characteristics of monopile foundations with riprap protection measures under current scour were studied in a flume through physical model experiments and three-dimensional numerical simulation methods in this research. It compared and analyzed the surrounding flow field characteristics, horseshoe vortex, wake vortex, and pressure distribution around the pile foundation in different scour stages under the influence of the current. The main conclusions are as follows:

(1) In the horizontal direction along the water flow direction, the maximum flow velocity around the piles continues to decrease during the riprap failure. After the stabilization of scour, the maximum flow velocities around the piles decrease to varying degrees, ranging from 9.32% to 17.05%.
(2) Compared with the unprotected monopile, the range of the horseshoe vortex in front of the pile with riprap protection increases obviously, and then decreases continuously during the failure of riprap. The wake vortex behind the pile maintains a relatively constant shape and size near the water surface during the failure of riprap, while the wake vortex near the riprap protection gradually becomes thinner and shorter, eventually disappearing.
(3) The pressure in front of the monopile is the largest, and the pressure values in front of the pile remain almost unchanged during the failure of riprap, while the pressure values at other positions show an increasing trend with varying magnitudes. When the scour is stable, the maximum pressure increase can reach 338% compared to the unprotected pile foundation.
(4) During the scour process, the wake vortex is the main change in the hydrodynamic characteristics between the riprap—protected monopile and the unprotected monopile, and the pressure changes on the pile should not be overlooked.

Thus, we recommend that when using the riprap protection, the damaged riprap layer should be repaired promptly. If the riprap is allowed to fail completely, the pressure on the lower part of the pile foundation will increase, putting the foundation in a more hazardous condition. It is worth exploring the combined use of riprap with other protective measures to further reduce the flow velocity in front of the pile, shrink the extent of the horseshoe vortex, and improve both the protective effectiveness and service life.

Author Contributions: Conceptualization, T.Y.; Methodology, T.Y., L.W. and C.M.; Software, L.W. and C.M.; Validation, T.Y.; Formal analysis, L.W.; Investigation, L.W. and X.D.; Writing—original draft, C.M.; Writing—review & editing, T.Y. and L.W.; Supervision, X.D. All authors have read and agreed to the published version of the manuscript.

Funding: This work was financially supported by the National Natural Science Foundation of China-Shandong Joint Fund (U2106224) and Shandong Provincial Natural Science Foundation (ZR2024ME251).

Data Availability Statement: The original contributions presented in this study are included in the article. Further inquiries can be directed to the corresponding author.

Conflicts of Interest: The authors declare no conflict of interest.

References

1. Blanco, M.I. The economics of wind energy. *Renew. Sustain. Energy Rev.* **2008**, *13*, 1372–1382. [CrossRef]
2. Sunday, K.; Brennan, F. A review of offshore wind monopiles structural design achievements and challenges. *Ocean Eng.* **2021**, *235*, 109409. [CrossRef]
3. Chambel, J.; Fazeres-Ferradosa, T.; Miranda, F.; Bento, A.; Taveira-Pinto, F.; Lomonaco, P. A comprehensive review on scour and scour protections for complex bottom-fixed offshore and marine renewable energy foundations. *Ocean Eng.* **2024**, *304*, 117829. [CrossRef]
4. Majumder, M.; Chakraborty, D. Effects of scour-hole depth on the bearing and uplift capacities of under-reamed pile in clay. *Ocean Eng.* **2021**, *240*, 109927. [CrossRef]
5. Li, J.; Guo, Y.; Lian, J.; Wang, H. Mechanisms, assessments, countermeasures, and prospects for offshore wind turbine foundation scour research. *Ocean Eng.* **2023**, *281*, 114893. [CrossRef]
6. Grimaldi, C.; Gaudio, R.; Calomino, F.; Cardoso, A.H. Countermeasures against local scouring at bridge piers: Slot and combined system of slot and bed sill. *J. Hydraul. Eng.* **2009**, *135*, 425–431. [CrossRef]
7. Lian, J.; Li, J.; Guo, Y.; Wang, H.; Yang, X. Numerical study on local scour characteristics of multi-bucket jacket foundation considering exposed height. *Appl. Ocean Res.* **2022**, *121*, 103092. [CrossRef]
8. Zhang, F.; Chen, X.; Yan, J.; Gao, X. Countermeasures for local scour around offshore wind turbine monopile foundations: A review. *Appl. Ocean Res.* **2023**, *141*, 103764. [CrossRef]
9. Parola, A.C. Stability of Riprap at Bridge Piers. *J. Hydraul. Eng.* **1993**, *119*, 1080–1093. [CrossRef]
10. Chiew, Y.M. Mechanics of Riprap Failure at Bridge Piers. *Int. J. Rock Mech. Min. Sci. Geomech. Abstr.* **1996**, *33*, 177. [CrossRef]
11. Chiew, Y.-M.; Lim, F.-H. Failure Behavior of Riprap Layer at Bridge Piers under Live-Bed Conditions. *J. Hydraul. Eng.* **2000**, *126*, 43–55. [CrossRef]
12. Lauchlan, C.S.; Melville, B.W. Riprap protection at bridge piers. *J. Hydraul. Eng.* **2001**, *127*, 412–418. [CrossRef]
13. Lim, F.-H.; Chiew, Y.-M. Parametric study of riprap failure around bridge piers. *Hydraul. Res.* **2001**, *39*, 61–72. [CrossRef]
14. Nielsen, A.W.; Probst, T.; Petersen, T.U.; Sumer, B.M. Sinking of armour layer around a vertical cylinder exposed to waves and current. *Coast. Eng.* **2015**, *100*, 58–66. [CrossRef]
15. Nielsen, A.W.; Sumer, B.M.; Fredsøe, J.; Christensen, E.D. Sinking of armour layer around a cylinder exposed to a current. *Proc. Inst. Civ. Eng. Marit. Eng.* **2011**, *164*, 159–172. [CrossRef]
16. Petersen, T.U.; Sumer, B.M.; Fredsøe, J.; Raaijmakers, T.C.; Schouten, J.-J. Edge scour at scour protections around piles in the marine environment —laboratory and field investigation. *Coast. Eng.* **2015**, *106*, 42–72. [CrossRef]
17. Nielsen, A.W.; Petersen, T.U. Stability of cover stones around a vertical cylinder under the influence of waves and current. *Coast. Eng.* **2019**, *154*, 103563. [CrossRef]
18. Whitehouse, R.J.S.; Harris, J.M.; Sutherland, J.; Rees, J. The nature of scour development and scour protection at offshore windfarm foundations. *Mar. Pollut. Bull.* **2011**, *62*, 73–88. [CrossRef]
19. de Almeida, G.A.M.; Martín-Vide, J.P. Riprap stability: Transverse and longitudinal versus continuous protections. *J. Hydraul. Eng.* **2009**, *135*, 447–456. [CrossRef]
20. Tang, Z.; Melville, B.; Shamseldin, A.Y.; Singhal, N.; Guan, D.; Stolte, A. Performance of riprap armour at vibrating offshore wind turbine monopile foundations. *Coast. Eng.* **2023**, *186*, 104392. [CrossRef]
21. De Vos, L.; De Rouck, J.; Troch, P.; Frigaard, P. Empirical design of scour protections around monopile foundations. Part 1: Static approach. *Coast. Eng.* **2011**, *58*, 540–553. [CrossRef]
22. De Vos, L.; De Rouck, J.; Troch, P.; Frigaard, P. Empirical design of scour protections around monopile foundations. Part 2: Dynamic approach. *Coast. Eng.* **2012**, *60*, 286–298. [CrossRef]
23. Richardson, E.V.; Davis, S.R. *Evaluating Scour at Bridges*; Federal Highway Administration: Washington, DC, USA, 2001.
24. Lagasse, P.F.; Clopper, P.E.; Zevenbergen, L.W.; Girar, L.G. *Countermeasures to Protect Bridge Piers from Scour*; Transportation Research Board; Ayres Associates Inc.: Fort Collins, CO, USA, 2007.
25. Wei, K.; Zhou, C.; Zhang, M.; Ti, Z.; Qin, S. Review of the hydrodynamic challenges in the design of elevated pile cap foundations for sea-crossing bridges. *Adv. Bridg. Eng.* **2020**, *1*, 21. [CrossRef]
26. Liu, M.; Zeng, L.; Wu, L.; Chen, G.; Shen, L.; Abi, E. In-Situ Test Method for Hydrodynamic Characteristics of Water Flowing Around Piles. *Front. Environ. Sci.* **2022**, *10*, 855334. [CrossRef]
27. Melville, B.W.; Coleman, S.E. *Bridge Scour*; Water Resources Publications: Littleton, CO, USA, 2000.
28. Kirkgoz, M.S.; Mehmet, A. Velocity profiles of developing and developed open channel flow. *J. Hydraul. Eng.* **1997**, *123*, 1099–1105. [CrossRef]
29. Roulund, A.; Sumer, B.M.; Fredsøe, J.; Michelsen, J. Numerical and experimental investigation of flow and scour around a circular pile. *J. Fluid Mech.* **2005**, *534*, 351–401. [CrossRef]

30. Hunt, J.; Wray, A.; Moin, P. *Eddies, Stream, and Convergence Zones in Turbulent Flows*; Center for Turbulence Research: Stanford, CA, USA, 1988; pp. 193–208.
31. Muzzammil, M.; Gangadhariah, T. The mean characteristics of horseshoe vortex at a cylindrical pier. *J. Hydraul. Res.* **2003**, *41*, 285–297. [CrossRef]